ELSEVIER

Gamma coincidence study of ^{208}Pb + 350 MeV ^{64}Ni collisions

W. Królas [a,*], R. Broda [a], B. Fornal [a], T. Pawłat [a], H. Grawe [b,1],
K.H. Maier [b], M. Schramm [b,2], R. Schubart [b,3]

[a] *H. Niewodniczański Institute of Nuclear Physics, Radzikowskiego 152, PL-31342 Kraków, Poland*
[b] *Hahn-Meitner-Institut, Glienicker Strasse 100, D-14109 Berlin 39, Germany*

Abstract

Products of ^{208}Pb + ^{64}Ni collisions at an energy 12% above the Coulomb barrier have been studied in a gamma spectroscopy thick target experiment. The product yield distribution has been established from the γ–γ coincidence analysis supplemented by target radioactivity measurements. Neutron evaporation from excited primary products has been estimated to determine the pre-emission map of fragments. We discuss the transfer of protons and neutrons between the colliding ions in terms of the N/Z ratio equilibration.
© 2003 Elsevier B.V. All rights reserved.

1. Introduction

Complex binary reactions which take place when two heavy ions collide at energies above the Coulomb barrier were in recent years successfully used for the spectroscopic

---

study of nuclei that are not accessible in standard fusion reactions (e.g., [1–4]). In thick target gamma–gamma coincidence experiments the excellent resolving power of Ge multi-detector arrays allows to select gamma transitions of a specific nucleus from the extremely complex spectrum of gamma rays that are emitted by a large number of collision products. In this type of study the analysis focuses on discrete lines representing gamma rays which are emitted from nuclear reaction products stopped in the target material and therefore are not affected by the Doppler effect. In fact, most of the nuclei produced in binary reactions are excited in the spin and energy range involving state life-times and/or feeding times substantially longer than the product stopping times; thus only a small part of gamma transitions escape detection due to the Doppler broadening.

Early application of the gamma coincidence analysis for the ^{60}Ni + ^{92}Mo colliding system demonstrated the possibility to identify fully the reaction exit channel, by detection of cross-coincidences between known gamma rays emitted from two excited fragments [5]. In spectroscopic application the observation of these gamma cross-coincidences was often used to identify new gamma rays and associate them with previously completely unknown yrast excitations in an isotopically assigned nucleus [2,4]. The richness of information available from the high quality gamma coincidence data was then subsequently unravelled by an extensive analysis performed for the neutron-deficient colliding system ^{54}Fe + ^{106}Cd [6]. It provided a complete distribution of production cross-sections for the individual fusion-evaporation and binary reaction products, the correlation of heavy and light fragments in binary reactions and it also displayed the main features of the angular momentum transfer to individual product nuclei. It has been shown that such studies can provide unique, exclusive information on mass, charge, energy and angular momentum transfer in heavy ion collisions.

The basic understanding of the reaction mechanism in heavy ion collisions was achieved by intense investigations employing various charged particle and heavy fragment detection techniques (see, e.g., [7,8] and references therein). In these studies the detailed knowledge of kinematics and dynamics allowed to extract conclusive information, which could never be obtained from the integrated gamma measurements. On the other hand it turned out that in practical application of deep-inelastic, massive transfer or incomplete fusion heavy ion reactions for the gamma spectroscopy studies the attained knowledge is not satisfactory enough and does not allow to predict details which are necessary for selection of optimal experimental conditions. Specifically, the trend to equilibrate the N/Z ratio of two colliding nuclei, which is one of the most important features determining the access to poorly studied neutron-rich nuclei, is known only in general terms [9–12]. Therefore, parallel to spectroscopic investigations aimed to study the excitation structure of selected neutron-rich nuclei, we performed a complete analysis of all gamma coincidence and radioactive decay data collected for the three heavy ion colliding systems, which represent distinctly different entrance channel conditions. This set of results gave us experimental knowledge which was used as a guide in planing other similar experiments. In the same time it allowed to shed new light on the N/Z ratio equilibration process in heavy ion collisions, which supplemented earlier knowledge. The results were already extensively discussed in Królas Ph.D. Thesis [13] and briefly summarized in Ref. [14]. The growing interest in using the deep-inelastic heavy ion reactions for nuclear spectroscopy justifies broader presentation of these results. In this initial paper we shall focus on details of the

analysis exemplified by procedures applied for the neutron-rich system ^{64}Ni + 350 MeV ^{208}Pb. The obtained secondary product yield distribution, reconstruction of the primary product map and the analysis of the N/Z equilibration process will be presented as a necessary introduction for a subsequent publication, in which all results, including those obtained for two other systems (^{58}Ni + ^{208}Pb, ^{64}Ni + ^{130}Te), general conclusions concerning the N/Z ratio equilibration and consequences for the nuclear spectroscopy applications will be discussed.

The ^{64}Ni + ^{208}Pb colliding system discussed in the present paper was studied already extensively by the charged particle detection techniques [15]. Whereas direct comparison of results obtained from so distinctly different experimental approaches is very difficult, the information available from these early studies gave essential background for our analysis. At various parts of the present work this information will be indicated and the complementary character of the contribution arising from the present gamma coincidence method will be summarised in the forthcoming paper.

2. Experiment and analysis

2.1. Experimental procedure

The 350 MeV ^{64}Ni beam from the VICKSI accelerator at HMI Berlin was focused on a 30 mg/cm^2 thick ^{208}Pb target isotopically enriched to 98.7%. The target chamber was located inside the OSIRIS γ-spectrometer which consisted of 11 Compton suppressed Ge detectors and an inner ball of 48 BGO elements. The γ–γ coincidences involved for each detector the energy and time signals with respect to the beam pulse and optionally the multiplicity and sum energy from the BGO ball. The cyclotron pulsing was set to 69 ns spacing between the beam bursts to allow for a clean separation of in- and off-beam events. The reaction products were stopped inside the target. Discrete gamma transitions not broadened by the Doppler effect were observed for deexcitation of states with half-life and/or feeding time longer than 2 ps.

After 84 hours of experiment the beam was stopped and the OSIRIS setup was switched to singles mode to observe the decay of radioactive products collected in the target. These measurements were continued for 3 days to acquire spectra of medium- and long-lived (1 h $< T_{1/2} <$ 70 days) radioactive isotopes. Afterwards the activity of the target was measured several times with a less efficient setup consisting of a single 80 cm^3 Ge(Li) detector in a passive low background lead shielding at the Institute of Nuclear Physics in Kraków. Last measurements were carried out 70 days after the experiment and were used for accurate identification of long-lived products ($T_{1/2} >$ 5 days).

2.2. Analysis of secondary product distribution

The analysis aimed at accurate determination of production yields for an as complete as possible set of secondary reaction products. Three independent and complementary methods were applied:
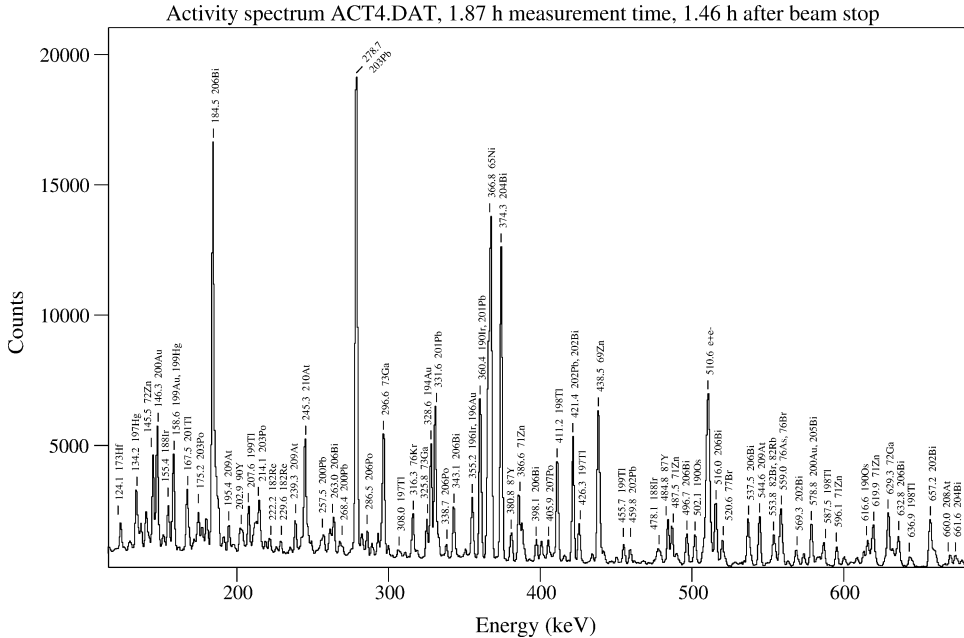
Fig. 1. Part of a radioactivity spectrum of the ^{208}Pb target irradiated for 84 h with 350 MeV ^{64}Ni beam. The measurement started 30 min after the beamtime end and was continued for 110 min. Strong lines are identified and labeled.

(1) The *quantitative analysis of the radioactive decay data* collected after experimental run at the HMI Berlin and those measured at the IFJ Krakow. It provided a basic set of rather precise values for medium- and long lived ($T_{1/2} > 1.5$ h) radioactive nuclei throughout all range of product distribution;

(2) The *off-beam gamma coincidence analysis* involving events between the beam pulses. Production yields of short-lived ($T_{1/2} < 1.5$ h) radioactive nuclides were determined for all cases, for which cascades of at least two gamma transitions appear in the radioactive decay. From this set of data also the population of isomeric states ($T_{1/2} > 10$ ns) was extracted.

(3) The *in-beam gamma coincidence analysis* was used to determine production yields of stable nuclei and of those undergoing radioactive decay not suited for gamma coincidence analysis.

In the analysis of complex radioactive decay spectra identification of the gamma lines were checked by following the decay through a time range of several half-lives. In Fig. 1 an example of the radioactivity gamma spectrum with indicated identifications is shown. Relative activity of each isotope at the time of irradiation end was calculated applying appropriate decay correction and using decay intensities from the Reus–Westmaier tables [16]. A fairly stable beam throughout all irradiation time simplified the extraction of relative yields in a broad range of half-lives: the shortest evaluated decay was the $T_{1/2} = 1.5$ h ^{78}As, the longest one was the 33.4 y ^{207}Bi. For half-lives longer than 12 h the
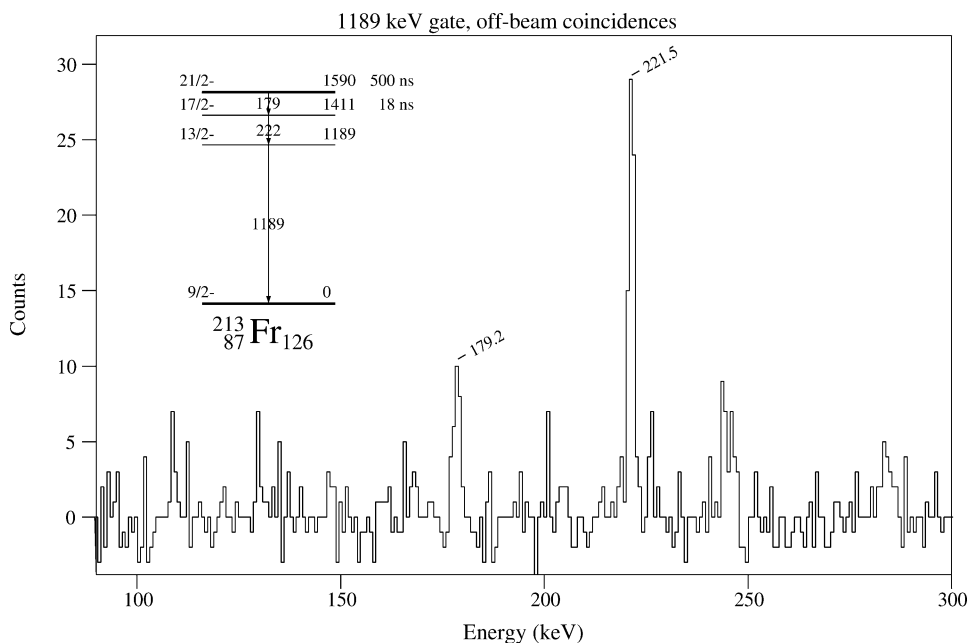
Fig. 2. Off-beam coincidence spectrum gated on 1189 keV transition from the decay of $21/2^-$ isomer in ^{213}Fr. Two other lines from the decay cascade are seen. A partial level scheme of ^{213}Fr is presented in the inset.

irradiation time was taken into account to extract yields from the activity which did not reach equilibrium level. In more complicated cases of direct production combined with population from a sequential decay more elaborate formulas were used to get the production yield of each individual nucleus. The number of radioactive decays observed in both HMI Berlin and IFJ Krakow measurements were used to combine the short-lived and long-lived activity results. In all, production yields of 120 radioactive isotopes were established from the radioactive decay data.

In a similar way, by using several cases observed in both sets of data, the results for very short-lived isotopes obtained from the analysis of gamma–gamma coincidences between the beam bursts were normalized to the single spectra radioactivity measurements. The high selectivity of these off-beam coincidence events compensated for obvious reduction of statistics, especially for cases in which the decay schemes offered only weak intensity of coincident transitions. The detailed knowledge of decay schemes necessary to convert the measured coincidence intensity into production yield was based on the most recent Nuclear Data Sheets compilations. This procedure was applied to extract production yields of about 160 short-lived radioactive nuclei and relative population intensity of many isomeric states. Two examples of the off-beam gamma coincidence spectra obtained for particularly small production yield cases are shown in Figs. 2 and 3 to demonstrate the quality of the data.

The most difficult was the determination of yields from the in-beam gamma–gamma coincidence analysis; consequently it provided less accurate results. Not only the complexity of the data contributed to these difficulties, also the interpretation of in-beam
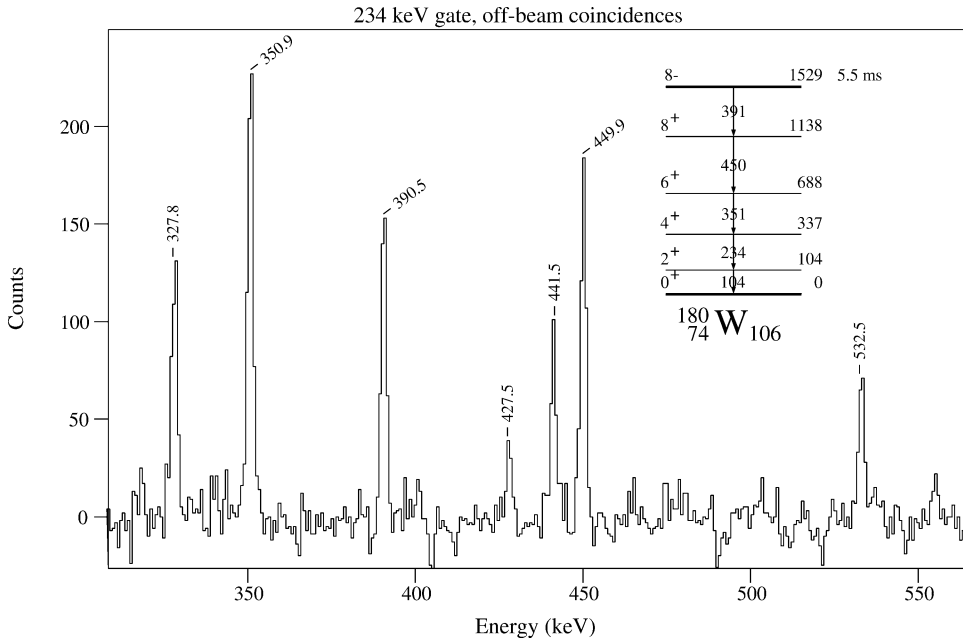
Fig. 3. Off-beam coincidence spectrum gated on 234 keV transition from the decay of 8^- isomer in ^{180}W. Three lines from the decay cascade are seen, other lines come from different contributions to the gate. A partial level scheme of ^{180}W is presented in the inset.

results required a knowledge of the population of various states in a given reaction product, i.e., one needed to estimate how much of the total production yield is represented by the coincidence intensity of two specific transitions in each analyzed nucleus. This was particularly important for nuclei produced in the vicinity of the target and projectile, where quasielastic processes populate many non-yrast states. For deep-inelastic products it turned out that in the lowest excitation region the population is predominantly yrast and the coincidence intensity of the lowest lying yrast transitions represents the bulk of production yield. Specifically, for even–even fragments that arise in large mass transfer (say $\Delta A > 10$) the lowest $4^+ \rightarrow 2^+ \rightarrow 0^+$ cascade usually represented more than 90% of the population yield. In Fig. 4 an example of the in-beam gamma coincidence spectrum is shown for the ^{170}Yb isotope, which represents a truly massive transfer reaction product. In all analysis of in-beam data the results were controlled by the observation of higher lying transitions and, whenever necessary, by introducing corrections based on the similarity to neighboring isotopes, for which the state population pattern could be detected in a more complete way. Obvious difficulties encountered in these procedures are reflected by much larger uncertainties of the in-beam results, than those attributed to values obtained from the two previously described methods. It should be noted that for cases involving isomeric states the extracted earlier off-beam intensity was added to the in-beam population to account for the total production rate. A number of well defined values obtained for the same products from the in-beam coincidence analysis and from earlier radioactivity singles and coincidence data were used to normalize all production yields to common relative units,
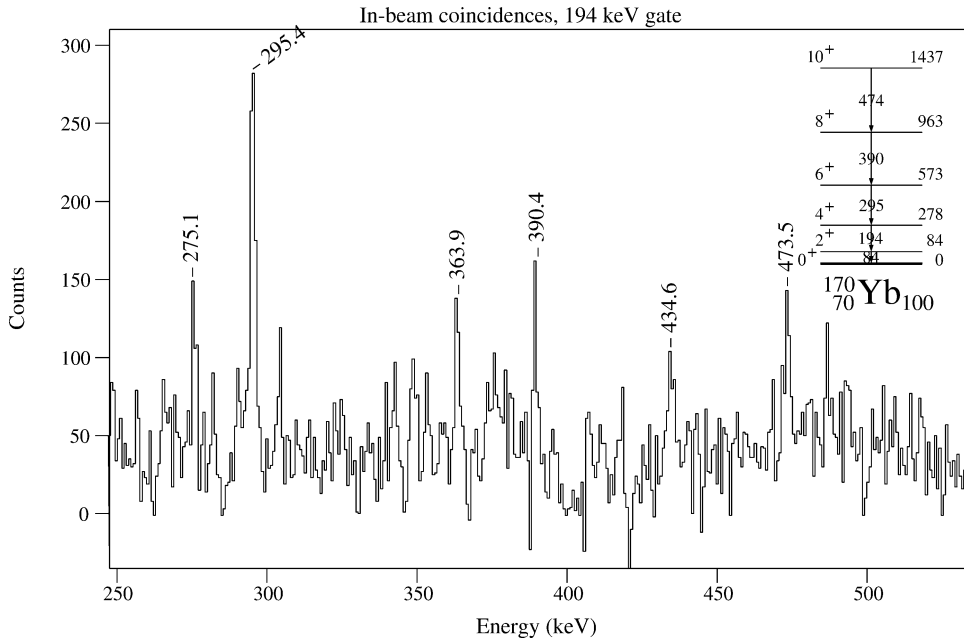
Fig. 4. In-beam coincidence spectrum gated on 194 keV $4^+ \to 2^+$ transition in ^{170}Yb. The 295, 390 and 474 keV lines from the same isotope are seen, several lines come from other contributions to the gate. A partial level scheme of ^{170}Yb is presented in the inset.

which were later converted to absolute cross section values as will be described in the following.

2.3. Absolute cross section normalization

The obtained final production yield distribution includes over 200 isotopes for which the relative production rates have been established with 10 to 30% accuracy taking into account all possible sources of errors. For another 40 isotopes we have set upper production rate limits. In order to convert these results into an absolute cross section scale we compared our results with the cross section values reported previously for similar colliding systems. Although such a cross section determination is not accurate (within 50% as we estimate) it enabled us to present the production yield results in microbarn units to give a direct sense of the population intensity.

The total reaction cross section for the ^{64}Ni + 1107 MeV ^{208}Pb inverse kinematic colliding system was determined by Sapotta et al. [15] from time-of-flight spectrometer measurements of light fragments. Converted into straight kinematic collisions this corresponds to 341 MeV ^{64}Ni projectile energy which is very close to the one used in our experiment. It is clear that our experimental gamma–gamma coincidence requirements eliminate elastic excitations of nuclei that were not counted into the cross section of reference. In our thick target measurement the beam energy was degraded in the target material down to the Coulomb barrier and consequently, our results relate to the average

Table 1
Total reaction cross section for ^{64}Ni and ^{208}Pb collisions

This work	K. Sapotta et al. [15]	σ_{react} [15]
^{208}Pb + 350 MeV ^{64}Ni	^{64}Ni + 1107 MeV ^{208}Pb	
$E_{CM} = 268$ MeV	$E_{CM} = 260$ MeV	1042 (70) mb

Table 2
Cross sections for one and two neutron transfer processes induced on ^{64}Ni projectiles in bombardments of ^{208}Pb target

Reaction	^{208}Pb + 380 MeV ^{64}Ni Ref. [17] (mb)[a]	^{208}Pb + 350 MeV ^{64}Ni his work (mb)
$(^{64}$Ni, ^{63}Ni)	60	56 (18)
$(^{64}$Ni, ^{65}Ni)	160	176 (16)
$(^{64}$Ni, ^{66}Ni)	40	50 (2)

[a] No errors given.

energy arising from the complete integration. The fact that our initial center-of-mass energy is by few MeV higher justifies a direct comparison with the Sapotta et al. results and yields a conservative estimate of 50% uncertainty for our absolute cross section scale.

In the normalization procedure the total reaction cross section of Ref. [15] (see Table 1) was compared to the half of the sum of production yields determined in our study (the balance between the heavy and light fragment yields was satisfactory). A normalization factor was obtained, that was used for presentation of the production yield results in an absolute cross section scale.

In order to confirm our production yield normalization we performed an additional check, comparing cross sections for population of specific nuclei obtained from our study with those reported by other authors. The transfer of one and two nucleons from/into light-medium projectiles bombarding a ^{208}Pb target has attracted special interest and was extensively investigated before—see, for instance, [17] and references therein. In Table 2 we compare the cross section for $(^{64}$Ni, ^{63}Ni), $(^{64}$Ni, ^{65}Ni) and $(^{64}$Ni, ^{66}Ni) transfer reactions induced on a ^{208}Pb target reported in previous papers and obtained in this paper. The collision energy reported by Rehm et al. [17] given in Table 2 is somewhat higher than the one of our experiment. Furthermore, the restriction mentioned in the previous paragraph, regarding the integration of the collision energy down to the Coulomb barrier in case of thick target experiments applies to this comparison as well. Despite this limitations and due to rather flat excitation functions of the compared processes in the energy range above the Coulomb barrier there is a systematic agreement between the listed values that confirms our absolute cross section normalization.

2.4. Gamma cross-coincidence analysis

The good quality of the experimental data enabled an extensive analysis of the cross-coincidence relations between gamma rays emitted from two excited nuclei that appear simultaneously in the binary reaction exit channel [2,4,18]. Both final reaction products
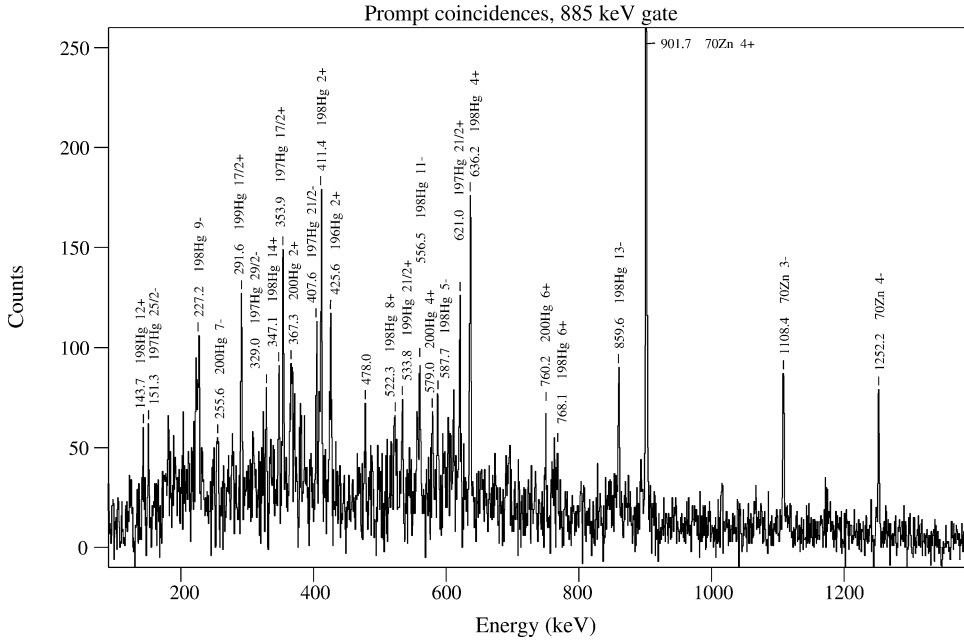
Fig. 5. In-beam coincidence spectrum gated on 885 keV $2^+ \rightarrow 0^+$ transition in ^{70}Zn. Strong lines from ^{70}Zn and from Hg partner nuclei are labeled.

are recognized by characteristic gamma ray energies, which provides full identification of the reaction, including direct information on the number of nucleons evaporated from the primary collision products. An example of a typical spectrum which served to analyze cross-coincidences is shown in Fig. 5. The gate set on the 885 keV $2^+ \rightarrow 0^+$ transition in ^{70}Zn gave a coincidence spectrum, which besides other lines of ^{70}Zn includes many gamma transitions that belong to Hg isotopes—complementary fragments that are formed by removal of two protons from the target. The observed gamma transitions from several Hg isotopes ranging from ^{200}Hg to ^{196}Hg define processes in which 2 to 6 neutrons are evaporated from the primary fragments in reactions producing the ^{70}Zn. In many favorable cases such analysis could be performed yielding reasonable control of the neutron evaporation process throughout all mass range of reaction products. This information was crucial to reconstruct the primary fragments distribution.

3. Distribution of secondary reaction products

The complete list of established reaction products is given in Tables 3 and 4. All values are given in microbarns. The errors reflect the uncertainty of the experimental procedure of relative yield determination, the uncertainty of the absolute cross section scaling is not included in the errors. The side feeding is subtracted for nuclei populated both directly and in the decay of other products. For radioactive isotopes with two decay branches the total yield value is given. Some hints on the method of analysis used for yield

Table 3
Light and medium-mass products of the ^{208}Pb + 350 MeV ^{64}Ni reaction. See text for details

Isotope	σ (μb)		Isotope	σ (μb)		Isotope	σ (μb)	
^{52}Ti	140 (60)	i.	^{61}Ni	180 (100)	i.	^{78}Ge	300 (300)	i.
^{53}Ti	< 80	f.	^{62}Ni	1300 (240)	i.	^{79}Ge	100 (100)	f.
^{53}V	< 250	i.	^{63}Ni	56000 (18000)	i.	^{73}As	200 (200)	f.
^{54}V	760 (120)	f.	^{64}Ni	560000 (60000)	i.	^{74}As	1000 (300)	a.
^{55}V	720 (400)	f.	^{65}Ni	176000 (16000)	a.	^{75}As	1600 (400)	e.
^{52}Cr	80 (80)	i.	^{66}Ni	50000 (2000)	a.	^{76}As	2200 (300)	a.
^{53}Cr	400 (200)	i.	^{67}Ni	4000 (1000)	f.	^{77}As	2400 (800)	f.
^{54}Cr	500 (100)	i.	^{68}Ni	1000 (200)	fi.	^{78}As	2300 (600)	f.
^{55}Cr	700 (200)	i.	^{69}Ni	80 (80)	f.	^{79}As	500 (200)	f.
^{56}Cr	1000 (120)	i.	^{62}Cu	< 100	fi.	^{80}As	200 (200)	f.
^{57}Cr	1300 (400)	i.	^{63}Cu	420 (120)	i.	^{75}Se	200 (200)	a.
^{58}Cr	400 (400)	e.	^{64}Cu	1400 (200)	fi.	^{76}Se	640 (120)	i.
^{53}Mn	< 200	i.	^{65}Cu	3000 (2000)	i.	^{77}Se	1000 (400)	e.
^{54}Mn	360 (80)	a.	^{66}Cu	4800 (1000)	fi.	^{78}Se	1700 (400)	i.
^{55}Mn	380 (120)	i.	^{67}Cu	12000 (2000)	a.	^{79}Se	2000 (800)	e.
^{56}Mn	1600 (300)	a.	^{68}Cu	6200 (800)	f.	^{80}Se	2000 (200)	i.
^{57}Mn	2000 (600)	e.	^{69}Cu	6600 (1400)	f.	^{81}Se	1200 (400)	e.
^{58}Mn	2200 (600)	f.	^{70}Cu	1600 (160)	f.	^{82}Se	540 (140)	i.
^{59}Mn	3400 (600)	f.	^{71}Cu	150 (150)	f.	^{83}Se	200 (200)	f.
^{60}Mn	1080 (160)	f.	^{64}Zn	100 (60)	i.	^{80}Br	400 (400)	i.
^{61}Mn	600 (400)	f.	^{65}Zn	400 (200)	a.	^{81}Br	1200 (300)	f.
^{62}Mn	< 140	f.	^{66}Zn	2000 (200)	i.	^{82}Br	1740 (160)	a.
^{54}Fe	< 80	i.	^{67}Zn	3000 (1000)	i.	^{83}Br	1460 (240)	fi.
^{55}Fe	150 (150)	e.	^{68}Zn	4000 (2000)	i.	^{84}Br	520 (80)	f.
^{56}Fe	480 (120)	i.	^{69}Zn	5400 (600)	a.	^{85}Br	100 (100)	f.
^{57}Fe	200 (200)	e.	^{70}Zn	3000 (800)	i.	^{80}Kr	< 300	i.
^{58}Fe	760 (120)	i.	^{71}Zn	2600 (400)	a.	^{81}Kr	300 (200)	e.
^{59}Fe	7200 (800)	a.	^{72}Zn	2400 (200)	a.	^{82}Kr	860 (160)	i.
^{60}Fe	8000 (2000)	i.	^{73}Zn	1000 (600)	f.	^{83}Kr	1200 (300)	i.
^{61}Fe	10600 (1200)	f.	^{68}Ga	160 (160)	fi.	^{84}Kr	1500 (150)	fi.
^{62}Fe	10000 (4000)	i.	^{69}Ga	600 (300)	i.	^{85}Kr	1000 (400)	e.
^{63}Fe	10000 (4000)	f.	^{70}Ga	1000 (200)	fi.	^{86}Kr	640 (120)	i.
^{64}Fe	4000 (4000)	e.	^{71}Ga	2000 (1000)	i.	^{87}Kr	600 (400)	f.
^{57}Co	< 100	i.	^{72}Ga	3800 (600)	a.	^{88}Kr	40 (40)	f.
^{58}Co	240 (60)	a.	^{73}Ga	4200 (1000)	a.	^{82}Rb	500 (250)	f.
^{59}Co	600 (400)	i.	^{74}Ga	2400 (400)	f.	^{83}Rb	860 (140)	a.
^{60}Co	3200 (200)	a.	^{75}Ga	600 (240)	f.	^{84}Rb	1360 (140)	a.
^{61}Co	7000 (8000)	f.	^{76}Ga	240 (120)	f.	^{85}Rb	600 (400)	fi.
^{62}Co	16000 (6000)	f.	^{71}Ge	300 (300)	e.	^{86}Rb	2000 (1000)	a.
^{63}Co	26000 (8000)	f.	^{72}Ge	600 (400)	i.	^{87}Rb	600 (200)	fi.
^{64}Co	16000 (4000)	f.	^{73}Ge	1000 (400)	i.	^{88}Rb	960 (320)	f.
^{65}Co	2000 (2000)	e.	^{74}Ge	1600 (240)	i.	^{89}Rb	340 (80)	f.
^{66}Co	200 (60)	f.	^{75}Ge	1100 (400)	a.	^{90}Rb	320 (140)	f.
^{59}Ni	< 160	i.	^{76}Ge	1600 (300)	i.	^{84}Sr	120 (80)	i.
^{60}Ni	120 (60)	i.	^{77}Ge	680 (100)	f.	^{85}Sr	800 (400)	a.

(*continued*)

Table 3 (*Continued*)

Isotope	σ (µb)		Isotope	σ (µb)		Isotope	σ (µb)	
^{86}Sr	800 (200)	fi.	^{94}Nb	700 (300)	e.	^{110}Ag	320 (60)	a.
^{87}Sr	600 (300)	i.	^{95}Nb	1160 (300)	a.	^{114}Cd	320 (120)	i.
^{88}Sr	820 (140)	i.	^{96}Nb	760 (80)	a.	^{116}In	340 (120)	f.
^{89}Sr	600 (200)	i.	^{97}Nb	600 (200)	e.	^{117}In	200 (80)	f.
^{90}Sr	600 (160)	i.	^{98}Nb	540 (120)	f.	^{118}In	180 (80)	f.
^{91}Sr	200 (200)	e.	^{99}Nb	320 (120)	f.	^{112}Sn	80 (60)	f.
^{84}Y	60 (40)	f.	^{100}Nb	220 (120)	f.	^{113}Sn	380 (200)	a.
^{85}Y	150 (150)	f.	^{94}Mo	40 (20)	f.	^{114}Sn	40 (20)	f.
^{86}Y	800 (200)	a.	^{95}Mo	460 (300)	i.	^{116}Sn	120 (60)	f.
^{87}Y	1300 (200)	a.	^{96}Mo	200 (100)	i.	^{117}Sn	180 (80)	a.
^{88}Y	200 (160)	a.	^{97}Mo	220 (60)	i.	^{118}Sn	360 (120)	f.
^{89}Y	220 (100)	i.	^{98}Mo	520 (120)	i.	^{120}Sn	240 (100)	f.
^{90}Y	560 (80)	a.	^{99}Mo	640 (120)	a.	^{122}Sn	60 (40)	f.
^{91}Y	200 (200)	e.	^{100}Mo	340 (60)	i.	^{120}Sb	240 (60)	a.
^{89}Zr	160 (80)	a.	^{99}Tc	300 (100)	i.	^{122}Sb	260 (40)	a.
^{90}Zr	100 (100)	f.	^{99}Ru	< 140	i.	^{124}Sb	180 (40)	a.
^{91}Zr	200 (200)	fi.	^{100}Ru	180 (60)	i.	^{121}Te	720 (100)	a.
^{92}Zr	620 (120)	i.	^{101}Ru	160 (80)	f.	^{123}Te	240 (120)	a.
^{93}Zr	600 (400)	e.	^{102}Ru	420 (100)	i.	^{124}I	220 (20)	a.
^{94}Zr	700 (300)	i.	^{103}Ru	1200 (200)	a.	^{127}Xe	280 (60)	a.
^{95}Zr	1080 (100)	a.	^{104}Ru	240 (100)	i.	^{139}Ce	580 (60)	a.
^{96}Zr	360 (180)	i.	^{101}Rh	60 (20)	a.	^{141}Ce	360 (60)	a.
^{90}Nb	100 (40)	a.	^{105}Rh	1000 (200)	a.	^{143}Pm	650 (200)	a.
^{91}Nb	100 (100)	e.	^{106}Pd	480 (120)	i.	^{148}Pm	320 (80)	a.
^{92}Nb	200 (200)	i.	^{108}Pd	420 (120)	i.			
^{93}Nb	480 (180)	i.						

determination of specific isotopes are given in the last column using the following symbols: a. yield established from radioactivity measurements, f. from off-beam gamma coincidence analysis, i. from in-beam coincidences, fi. both off- and in-beam coincidence date were used. For some nuclei any experimental analysis is very difficult or impossible due to the lack of spectroscopic information. In such a case the production yield is interpolated basing on firm results obtained for neighboring nuclei—such values are marked in the tables by e. "estimated" note. For regions of lowest population intensity no estimation can be done as only scattered results are available for isotopes which can be detected with the highest sensitivity (e.g., those with favorable decay conditions). For a more detailed report on the ^{208}Pb + 350 MeV ^{64}Ni collision product distribution we refer to reference [13].

The location of the reaction products on the N–Z plane is displayed in Figs. 6 and 7 and the mass distribution of products is shown in Fig. 8. The detected products are binary fragments produced in deep-inelastic, inelastic and quasielastic processes. The distribution of those nuclei have maxima centered around the target and projectile but extend over a wide range of elements corresponding to increasing mass and charge transfer. The general trend to equilibrate the mass asymmetry of the colliding nuclei is obvious—the transfer of nucleons from the heavy into the light fragment is favored.

Table 4
Heavy fragments, products of the ^{208}Pb + 350 MeV ^{64}Ni reaction. See text for details

Isotope	σ (μb)		Isotope	σ (μb)		Isotope	σ (μb)	
^{154}Gd	< 80	i.	^{182}W	500 (150)	i.	^{191}Pt	4000 (400)	a.
^{156}Gd	140 (60)	i.	^{183}W	500 (300)	e.	^{192}Pt	4100 (500)	fi.
^{156}Tb	380 (40)	i.	^{184}W	400 (200)	fi.	^{193}Pt	3800 (600)	i.
^{160}Tb	< 250	a.	^{185}W	400 (200)	e.	^{194}Pt	3600 (400)	fi.
^{158}Dy	160 (60)	i.	^{186}W	320 (160)	i.	^{195}Pt	3000 (1000)	e.
^{160}Dy	320 (100)	i.	^{187}W	260 (60)	a.	^{196}Pt	1800 (400)	i.
^{162}Dy	100 (60)	i.				^{197}Pt	600 (600)	e.
			^{179}Re	< 150	f.	^{198}Pt	< 200	fi.
^{162}Er	100 (60)	i.	^{180}Re	320 (160)	f.			
^{164}Er	340 (100)	i.	^{181}Re	1160 (120)	a.	^{190}Au	< 500	f.
^{166}Er	200 (60)	i.	^{182}Re	1040 (160)	a.	^{191}Au	1000 (200)	fi.
^{168}Er	160 (80)	i.	^{183}Re	1600 (400)	f.	^{192}Au	1800 (200)	a.
^{168}Tm	950 (150)	a.	^{184}Re	2400 (1000)	a.	^{193}Au	2400 (400)	fi.
			^{185}Re	2200 (600)	fi.	^{194}Au	5200 (600)	a.
^{166}Yb	200 (40)	a.	^{186}Re	2000 (1000)	e.	^{195}Au	6700 (1000)	a.
^{167}Yb	400 (200)	e.	^{187}Re	2000 (1000)	fi.	^{196}Au	5400 (400)	a.
^{168}Yb	540 (180)	fi.	^{188}Re	1600 (400)	a.	^{197}Au	3000 (1500)	f.
^{169}Yb	1100 (150)	a.	^{189}Re	1600 (300)	a.	^{198}Au	2440 (320)	a.
^{170}Yb	1000 (200)	fi.	^{190}Re	< 200	f.	^{199}Au	1420 (160)	a.
^{171}Yb	800 (400)	e.				^{200}Au	< 400	f.
^{172}Yb	600 (200)	fi.	^{182}Os	200 (80)	fi.			
^{173}Yb	200 (200)	e.	^{183}Os	500 (300)	e.	^{192}Hg	< 100	i.
^{174}Yb	< 100	i.	^{184}Os	1000 (400)	fi.	^{193}Hg	280 (60)	i.
^{170}Lu	1100 (200)	a.	^{185}Os	2400 (300)	a.	^{194}Hg	1400 (300)	fi.
^{171}Lu	1350 (150)	a.	^{186}Os	2200 (400)	fi.	^{195}Hg	2200 (400)	i.
^{172}Lu	1060 (120)	a.	^{187}Os	1700 (500)	i.	^{196}Hg	5400 (800)	fi.
			^{188}Os	2400 (500)	fi.	^{197}Hg	5000 (800)	a.
^{172}Hf	< 150	fi.	^{189}Os	1600 (600)	e.	^{198}Hg	6800 (800)	i.
^{173}Hf	500 (60)	a.	^{190}Os	1000 (200)	fi.	^{199}Hg	4000 (800)	f.
^{174}Hf	600 (300)	f.	^{191}Os	1300 (400)	a.	^{200}Hg	4300 (400)	i.
^{175}Hf	1200 (600)	a.	^{192}Os	140 (80)	f.	^{201}Hg	2500 (500)	f.
^{176}Hf	800 (120)	fi.				^{202}Hg	2200 (400)	i.
^{177}Hf	600 (300)	f.	^{184}Ir	< 400	f.	^{203}Hg	520 (80)	a.
^{178}Hf	600 (200)	f.	^{185}Ir	720 (200)	a.	^{204}Hg	540 (80)	i.
^{179}Hf	1100 (150)	ai.	^{186}Ir	900 (100)	a.	^{205}Hg	< 200	fi.
^{180}Hf	80 (60)	fi.	^{187}Ir	1200 (400)	i.	^{206}Hg	< 120	fi.
^{181}Hf	< 150	a.	^{188}Ir	2000 (200)	a.			
^{178}Ta	550 (100)	f.	^{189}Ir	3000 (400)	fi.	^{195}Tl	< 400	i.
^{179}Ta	550 (150)	f.	^{190}Ir	2700 (300)	a.	^{196}Tl	800 (800)	e.
^{180}Ta	700 (400)	e.	^{191}Ir	1920 (240)	fi.	^{197}Tl	3200 (500)	f.
^{181}Ta	700 (400)	e.	^{192}Ir	620 (60)	a.	^{198}Tl	3900 (1000)	f.
^{182}Ta	800 (400)	a.	^{193}Ir	440 (200)	e.	^{199}Tl	4400 (800)	a.
^{183}Ta	950 (150)	a.	^{194}Ir	320 (80)	a.	^{200}Tl	5400 (600)	f.
^{184}Ta	320 (80)	f.	^{195}Ir	< 200	f.	^{201}Tl	10800 (1000)	a.
^{178}W	350 (100)	i.	^{187}Pt	< 120	i.	^{202}Tl	8600 (800)	a.
^{179}W	800 (200)	fi.	^{188}Pt	600 (150)	a.	^{203}Tl	8400 (800)	fi.
^{180}W	1200 (200)	fi.	^{189}Pt	1200 (400)	i.	^{204}Tl	7800 (1800)	f.
^{181}W	1200 (600)	e.	^{190}Pt	2100 (300)	fi.	^{205}Tl	7200 (1200)	fi.

(*continued*)

Table 4 (*Continued*)

Isotope	σ (µb)		Isotope	σ (µb)		Isotope	σ (µb)	
206Tl	2260 (320)	fi.	201Bi	500 (120)	fi.	212Po	2900 (300)	fi.
207Tl	1260 (120)	f.	202Bi	1400 (300)	f.	206At	< 400	f.
208Tl	1000 (400)	f.	203Bi	2800 (400)	a.	207At	660 (180)	fi.
209Tl	< 20	f.	204Bi	5200 (700)	a.	208At	1550 (200)	fi.
197Pb	< 120	fi.	205Bi	8000 (1000)	a.	209At	2200 (250)	a.
198Pb	520 (60)	f.	206Bi	8000 (1200)	f.	210At	3000 (200)	a.
199Pb	2000 (300)	fi.	207Bi	11200 (1000)	fi.	211At	3550 (500)	fi.
200Pb	2700 (300)	a.	208Bi	9000 (1000)	fi.	212At	1320 (300)	fi.
201Pb	4900 (500)	a.	209Bi	16700 (2000)	fi.	213At	620 (200)	f.
202Pb	8600 (1200)	fi.	210Bi	4000 (2000)	e.	209Rn	200 (100)	f.
203Pb	17700 (2000)	a.	211Bi	500 (120)	f.	210Rn	660 (80)	f.
204Pb	16000 (2000)	f.	202Po	80 (40)	f.	211Rn	1260 (100)	a.
205Pb	23000 (2500)	fi.	203Po	360 (160)	i.	210Rn	660 (80)	f.
206Pb	77000 (8000)	fi.	204Po	1000 (200)	f.	211Rn	1260 (100)	a.
207Pb	86000 (10000)	fi.	205Po	2600 (600)	f.	212Rn	1800 (300)	fi.
208Pb	96000 (10000)	fi.	206Po	4800 (400)	a.	213Rn	1500 (300)	f.
209Pb	22000 (2000)	i.	207Po	5200 (600)	a.	214Rn	1360 (120)	fi.
210Pb	2100 (200)	fi.	208Po	8900 (800)	fi.	212Fr	140 (60)	f.
211Pb	< 600	f.	209Po	13000 (1200)	fi.	213Fr	280 (40)	f.
199Bi	40 (40)	f.	210Po	15000 (1200)	fi.	214Ra	< 60	f.
200Bi	200 (100)	f.	211Po	1360 (360)	fi.			

A small contribution of binary fragments that originate from fission of some heavy reaction products was detected in the region of symmetric mass division (i.e., $96 \leqslant A \leqslant 128$). On the other hand, the fusion cross section is expected to be rather small for this system at a colliding energy 12% above the Coulomb barrier, since additional extra-push energy is required to form a compound system. It was found that the fusion induced on ^{208}Pb target becomes important at ^{64}Ni projectile energy of about 380 MeV [19]. Nevertheless, a few long lived radioactive products could be detected due to high sensitivity in the region around $A \approx 140$ corresponding to fusion–fission events.

It is important to notice that in the measurements we observe final fragments—isotopes that are created after the evaporation of particles from excited primary products. Since most of the produced nuclei are neutron-rich or situated on the stability line it is reasonable to assume that only neutrons are emitted from the primary fragments. Consequently, the evaporation process shifts the distribution of fragments towards stable and neutron deficient nuclei.

The ^{64}Ni projectile nucleus lies on the neutron-rich side of the stability line (stable nuclei are marked by thick framelines in Figs. 6 and 7). Nevertheless, the projectile easily accepts additional neutrons from the heavy reaction partner. Exotic, neutron-rich fragments such as ^{68}Ni, ^{69}Ni were identified in the data. In processes that involve transfer of protons also the neutron-rich nuclei are populated. However, at larger mass transfer the final product distribution moves back towards the stability region. This effect, as will be discussed later, is clearly connected with the N/Z equilibration process and with the evaporation of neutrons from primary reaction products.
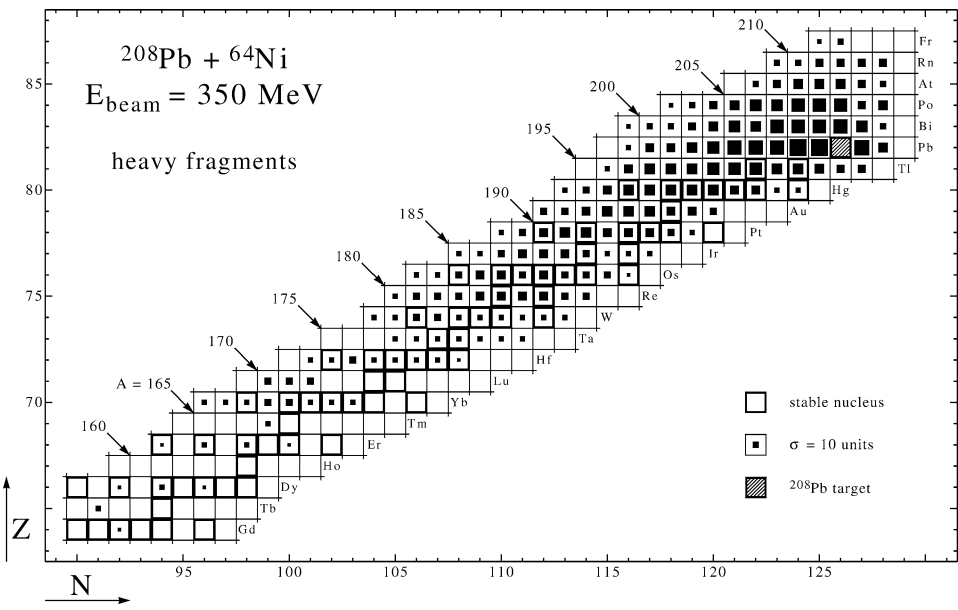
Fig. 6. Distribution of heavy fragments produced in ^{208}Pb + 350 MeV ^{64}Ni collisions.
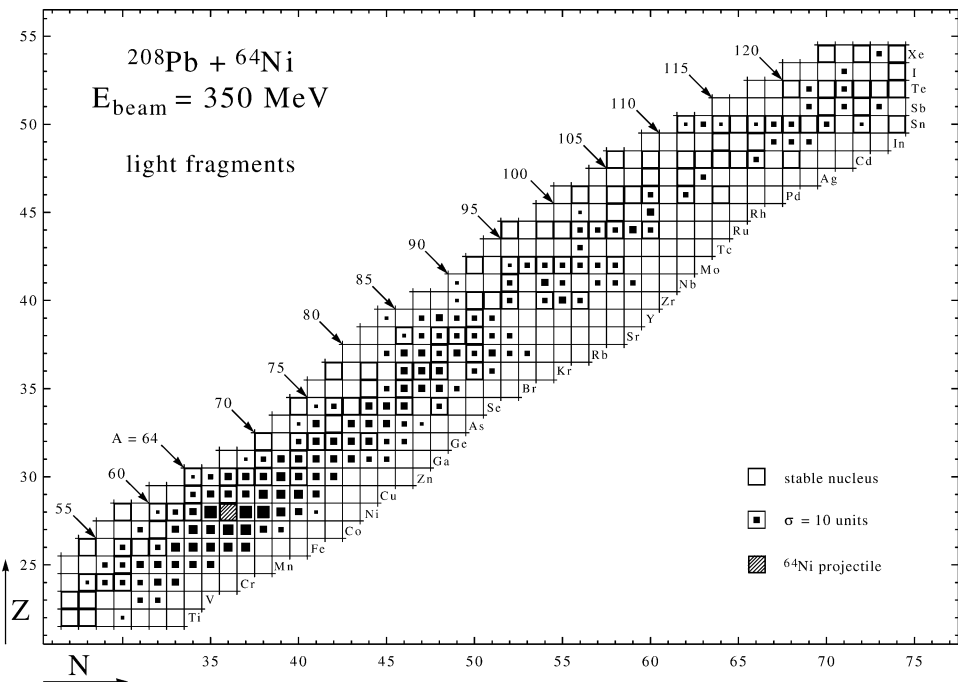

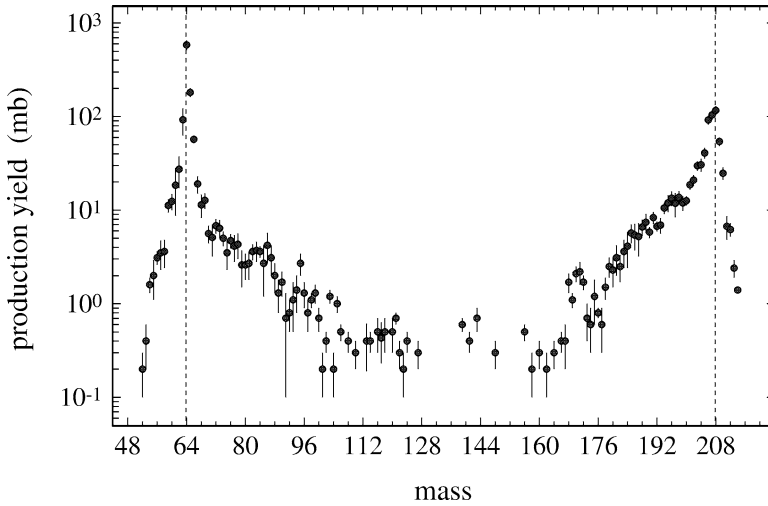Fig. 7. Distribution of light and medium-mass fragments produced in ^{208}Pb + 350 MeV ^{64}Ni collisions.

Fig. 8. Mass distribution of fragments produced in ^{208}Pb + 350 MeV ^{64}Ni collisions. The dashed lines indicate the mass of the projectile and target nuclei.

A long tail of the heavy fragments distribution extends down to rare earth nuclei indicating that transfers of up to 40 nucleons take place. The population yield decreases in case of the most massive transfers, for isotopes of Lu ($Z = 71$) and lighter ones it is in the range of our detection limit. Consequently, for this mass region, the experimental map of products includes only selected nuclei, which can be more easily detected (e.g., even–even nuclei from in-beam coincidences or long-lived radioactive products).

The distribution of light fragments presented in Fig. 7 is even more extended than that of the heavy ones. As mentioned earlier this is due to the products arising from the subsequent fission of some heavy fragments produced in deep-inelastic reactions and/or from the very weak fusion–fission reaction channel. One may notice that for fragments heavier than $A = 90$, the yield information is limited to selected isotopes due to low population intensities. Nevertheless, our interpretation is confirmed by the results obtained from another study of ^{208}Pb + ^{58}Ni collisions where this group of products appears more prominently [13].

In Fig. 8 the mass distribution of both target-like and projectile-like fragments is presented.

4. Primary product distribution

Most of the fragments established in the experimental analysis are located on the neutron rich side of the stability path or on the stability path itself. For that reason, it is safe to assume that the emission of particles from the hot primary products is limited to neutron evaporation. The emission of protons and other charged particles from the neutron rich fragments is unlikely and thus can be neglected.

The proposed reproduction of primary fragment distribution consists of an isotope dependent mass shift towards more neutron-rich nuclei. The isotope dependance of the mass shift is especially important for nuclei in the vicinity of the target and projectile nucleus. This is due the contribution of quasielastic processes in which the excitation energy of the primary products is smaller than the average one. The importance of such differential correction decreases at larger mass distance from the target and projectile. The analysis of gamma–gamma cross coincidences described in Section 2.4 provides direct experimental input to introduce the isotope dependent mass shift that correctly transforms the measured secondary product distribution into the primary one.

The observed cross coincidences analysed quantitatively gave the distribution of intensities (or probabilities) with which the partner nuclei appear in the reaction exit channel together with the selected isotope. In Fig. 9 we show results of such an analysis for the Pb–Ni combination of elements, complementary reaction products. Gates set on the most intense gamma transitions in various Ni isotopes displayed gamma lines from corresponding Pb reaction partners. The extracted intensities were used to estimate their probability of appearance together with the selected Ni isotope. Consequently, by weighting each partner mass with the cross coincidence yield one can deduce the average number of neutrons evaporated in all processes that contribute to the production of a given Ni isotope. This tedious procedure was performed both ways and the right-hand side of Fig. 9 shows yield distributions of Ni isotopes cross coincident with various Pb products. For other combinations of complementary elements only the latter way, i.e., the heavy partner gating was completely analysed. It allowed us to deduce the correction for neutron evaporation of the heavy fragment distribution, that was in our case more complete and reliable than the light fragment part. It has to be pointed out that even this sophisticated analysis cannot distinguish which of the two partners emitted neutrons. Thus the obtained total number of evaporated neutrons had to be divided between the heavy and light partners. Doing this we assumed that the excitation energy, and so the number of emitted neutrons is shared between the fragments proportionally to their mass.

The scheme of reconstruction of the primary heavy product distribution from the observed secondary products map is shown in Fig. 10. One can read from it that the integral production of, e.g., ^{207}Pb arises in processes in which on the average 0.7 neutron was evaporated from the heavy partner, average 1.3 neutron evaporation accompanied the production of ^{206}Pb, 2.0 neutron for ^{205}Pb etc.

It is to be noticed that for elements lighter than Pt (Ir, Os etc.), no isotope dependent correction is deduced due to low cross-coincidence statistics for those less abundant fragments. For those and still lighter elements we apply the so-called missing mass correction. We calculate the number of missing neutrons by subtracting the yield weighted masses of isotopes of two complementary elements from the $A = 272$ total mass of the colliding system. This number of missing neutrons is divided between the light and heavy complementary fragments according to their mass balance. The missing mass correction is appropriate for products far from the target and projectile nuclei since individual isotope-to-isotope differences in the number of evaporated neutrons are averaged for processes which involve transfer of many nucleons.

The right side of Fig. 10 shows numbers obtained from calculating the yield weighted average neutron evaporation for all isotopes of a given element. This is compared to the
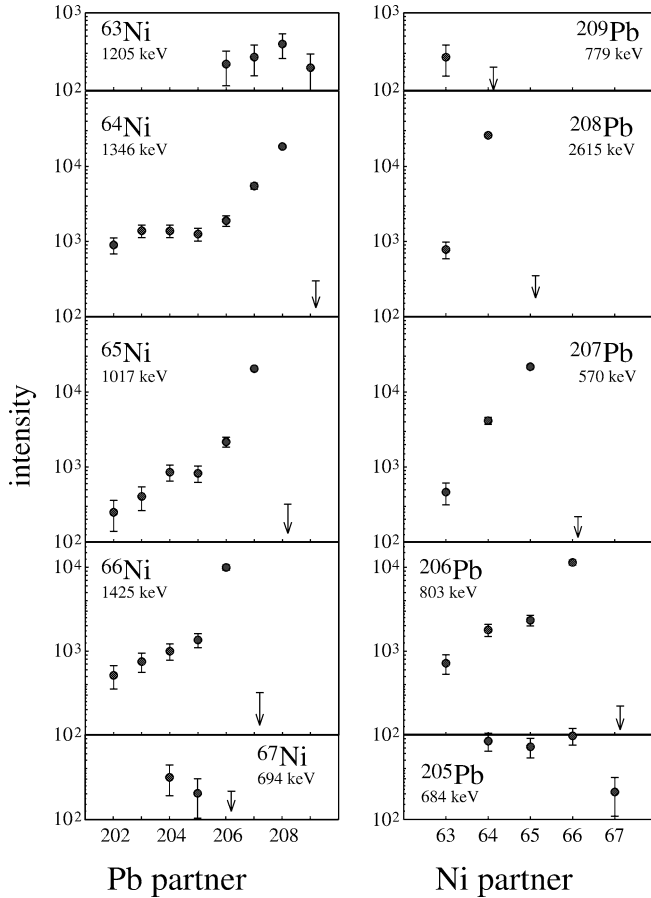
Fig. 9. Results of the cross coincidence analysis for Ni and Pb isotopes. Gates are set on most intense gamma transitions in Ni (left side) and Pb (right side) isotopes. The points indicate relative yields of partner nuclei produced in coincidence. Intensity limits are indicated by arrows for cases in which no cross coincidences were seen.

numbers obtained from the missing mass analysis. The agreement of both values indicates that the deduced scheme for accounting the neutron evaporation is indeed reliable.

5. Equilibration of the N/Z ratio

To investigate this aspect of mass and charge flow we calculated from the distribution of primary products the average value of the N/Z ratio for isobars at each mass—see Fig. 11. It is clearly seen that even a small transfer of mass leads to a partial but significant equilibration of the neutron-to-proton ratio. Further flow of mass does not change the almost constant N/Z level. The strong contribution of quasielastic processes dominates the results for points that are close to the target and projectile masses. The plot of Fig. 11

^{208}Pb + 350 MeV ^{64}Ni
heavy fragments

	evaporated neutrons from c-c, m-mass	
Fr	3.5	3.8(10)
Rn	3.0	3.2(4)
At	3.3	3.1(2)
Po	2.0	1.7(3)
Bi	1.7	1.8(2)
Pb	1.1	1.0(2)
Tl	2.6	2.2(2)
Hg	3.1	3.5(3)
Au	3.2	3.2(2)
Pt	3.3	3.4(4)
Ir		4.6(3)
Os		4.1(3)

Fr: 212Fr 3.5 n, 213Fr 3.5 n

Rn: 209Rn 4.0 n, 210Rn 3.6 n, 211Rn 3.2 n, 212Rn 3.0 n, 213Rn 2.7 n, 214Rn 2.4 n

At: 207At 4.0 n, 208At 3.8 n, 209At 3.6 n, 210At 3.3 n, 211At 3.0 n, 212At 2.7 n, 213At 2.4 n

Po: 202Po 4.8 n, 203Po 4.4 n, 204Po 4.0 n, 205Po 3.5 n, 206Po 3.1 n, 207Po 2.8 n, 208Po 2.2 n, 209Po 1.8 n, 210Po 1.3 n, 211Po 0.8 n, 212Po 0.2 n

Bi: 199Bi 5.5 n, 200Bi 5.5 n, 201Bi 5.0 n, 202Bi 4.5 n, 203Bi 3.9 n, 204Bi 3.3 n, 205Bi 2.7 n, 206Bi 2.2 n, 207Bi 1.7 n, 208Bi 1.1 n, 209Bi 0.5 n, 210Bi 0.0 n, 211Bi 0.0 n

Pb: 198Pb 5.6 n, 199Pb 5.5 n, 200Pb 5.4 n, 201Pb 4.7 n, 202Pb 4.1 n, 203Pb 3.4 n, 204Pb 2.7 n, 205Pb 2.0 n, 206Pb 1.3 n, 207Pb 0.7 n, 208Pb 0.0 n, 209Pb 0.0 n, 210Pb 0.0 n

Tl: 196Tl 5.0 n, 197Tl 4.6 n, 198Tl 4.4 n, 199Tl 4.1 n, 200Tl 3.9 n, 201Tl 3.2 n, 202Tl 2.7 n, 203Tl 2.1 n, 204Tl 1.5 n, 205Tl 1.0 n, 206Tl 0.4 n, 207Tl 0.0 n, 208Tl 0.0 n

Hg: 193Hg 5.5 n, 194Hg 5.2 n, 195Hg 4.7 n, 196Hg 4.1 n, 197Hg 3.7 n, 198Hg 3.2 n, 199Hg 2.7 n, 200Hg 2.3 n, 201Hg 1.7 n, 202Hg 1.3 n, 203Hg 0.8 n, 204Hg 0.3 n

Au: 191Au 4.6 n, 192Au 4.3 n, 193Au 4.0 n, 194Au 3.6 n, 195Au 3.3 n, 196Au 3.0 n, 197Au 2.6 n, 198Au 2.3 n, 199Au 2.0 n

Pt: 188Pt 4.5 n, 189Pt 4.2 n, 190Pt 4.0 n, 191Pt 3.7 n, 192Pt 3.5 n, 193Pt 3.2 n, 194Pt 3.0 n, 195Pt 2.7 n, 196Pt 2.5 n, 197Pt 2.2 n
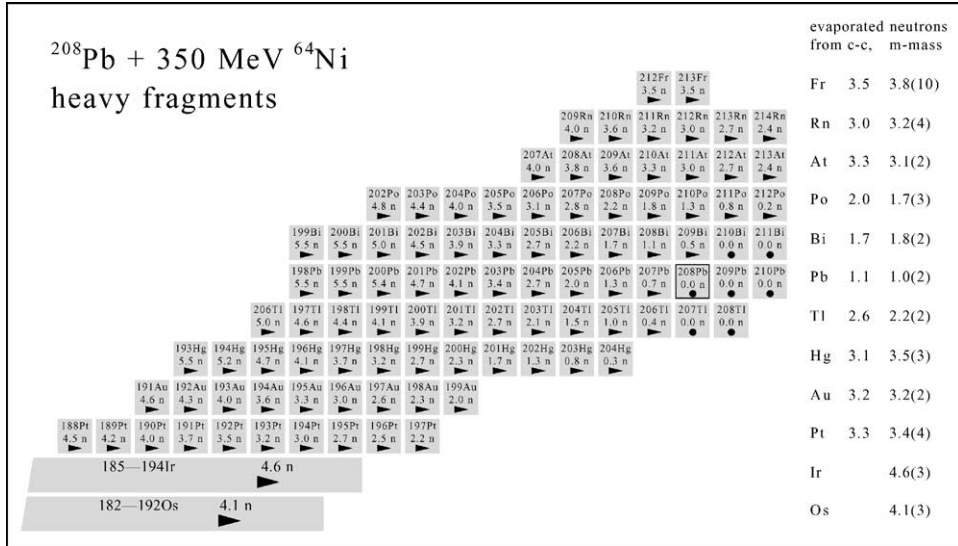
Ir: 185—194Ir 4.6 n

Os: 182—192Os 4.1 n

Fig. 10. Scheme of reconstruction of the primary distribution of heavy products obtained from cross coincidence analysis. For each secondary product an average number of neutrons evaporated in all processes that contributed to the formation of this isotope is given. In the right part of the figure, average numbers of neutrons evaporated from isotopes of a specific element are given.

includes two sets of points. The results obtained for sharing the evaporated neutrons between the two fragments proportional to their mass are indicated by solid circles whereas values obtained assuming equal sharing of neutrons are marked by the open triangles.

Some general concepts on neutron-to-proton ratio equilibration in heavy ion collisions were given as early as in 1972 in a review by Swiatecki [9]. The author pointed out that if two nuclei with differing N/Z ratios are brought into contact, a redistribution of neutron and proton densities should take place. Consequently, he derived an equilibration formula for the optimum N/Z value of fragments of a given mass, assuming the minimization of the liquid drop energy of two touching spherical nuclei. Recently, after consideration of the N/Z equilibration results of this work, Swiatecki suggested that a more general approach that involves the possible configuration of distant, non-touching nuclei at scission point, might give a better account of the observed effects [20]. The key point of this suggestion was the assumption that during the collision both nuclei may attain strongly deformed shape. The distant spheres in a very crude way can imitate such deformation effect since it simulates appropriately the Coulomb repulsion which is the most significant part of the minimized energy.

In Fig. 12 the experimental results are compared to the equilibration formula calculation (presented in detail in reference [13]). Data points corrected for neutron evaporation assuming both mass proportional (upper plot) and equal (lower plot) partition are shown. The dashed lines are drawn for a $d = 12$ fm touching spheres configuration. The values denoted by solid lines are obtained for a $d > 12$ fm distant spheres calculation. The d parameter, which is the distance between the centers of two spherical nuclei was adjusted to fit the experimental data. Its value depends strongly on the assumed partition of evaporated
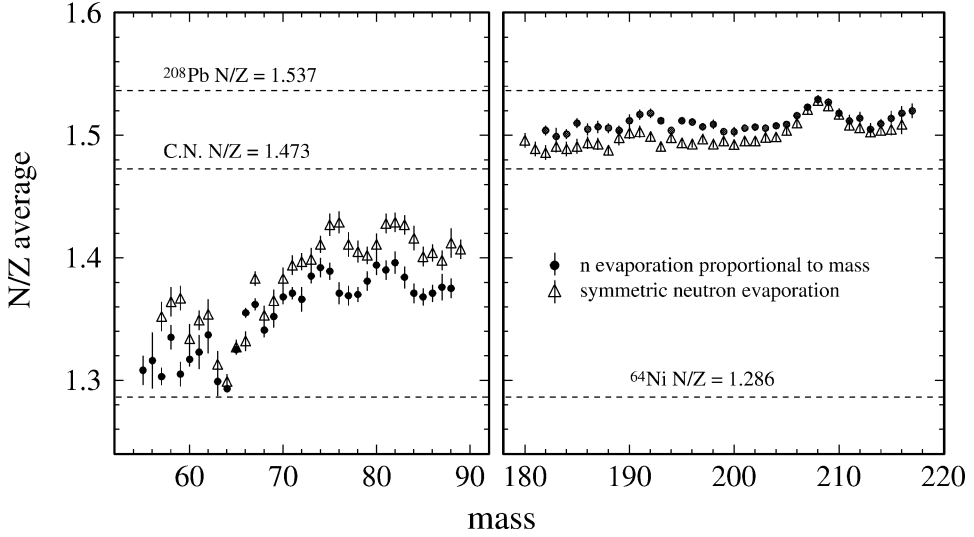
Fig. 11. Experimental N/Z values as a function of the fragments mass. The solid circles indicate the results obtained for proportional to the mass sharing of the evaporated neutrons between the two fragments. The open triangles were obtained if equal partition of evaporated neutrons between two fragments was assumed. Dashed lines are drawn to indicate the N/Z ratios of the target, projectile and compound system.
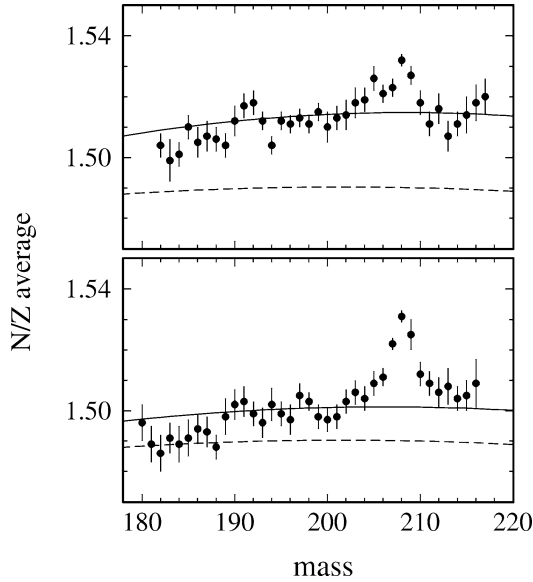

Fig. 12. Equilibration of the N/Z ratio for heavy fragments. Presented results are corrected for neutron evaporation assuming proportional to mass (upper plot) and equal (lower plot) neutron partition. The dashed lines follow the equilibration formula for $d = 12$ fm touching spheres configuration. The solid lines show the best fits of the equlibration formula to experimental data with $d = 22$ fm (upper plot) and $d = 15$ fm (lower plot) distance parameters obtained in the fitting procedure.
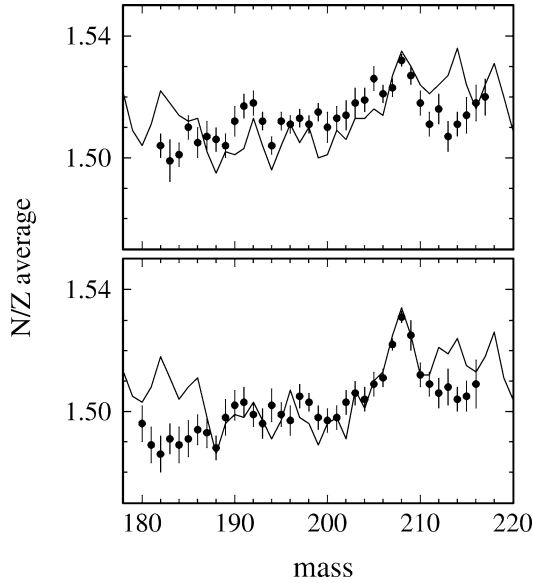
Fig. 13. Equilibration of the N/Z ratio for heavy fragments. Experimental values were corrected for neutron evaporation assuming proportional to mass (upper plot) and equal (lower plot) neutron partition. The lines are results of total energy minimization which includes experimental nuclear masses. Fits of the distance parameter to the experimental data of the upper and lower plot, produced values of $d = 22$ fm and 18 fm, respectively.

neutrons. Separation distance values of $d = 22$ fm for the upper plot data and $d = 15$ fm for the lower plot data, were obtained. It is apparent that the assumption of equal partition of evaporated neutrons allows to reproduce the N/Z equilibration at much smaller separation of nuclear spheres, which corresponds to less significant deformation.

The equilibration formula accounts for the general trend of the proton and neutron redistribution. However, since the liquid drop formula describes only the average properties one cannot expect an overall exact agreement, in particular any observed fluctuations of the experimental N/Z cannot be reproduced. We therefore tried another procedure involving an analogous minimization of the total energy (reaction Q-value and Coulomb interaction) that involves experimentally determined nuclear masses [21]. The Coulomb repulsion term was calculated assuming a spherical system (touching spheres) or a deformed one, consisting of two distant spheres connected by tangent cones. In Fig. 13 results of such total energy minimization are compared with the experimental values. Essentially the agreement with experimental values is of the same quality as discussed previously and reproduction of some fluctuations seems to be accidental. The following d parameter values were obtained from fits to the data: $d = 22$ fm for proportional to the mass partition of evaporated neutrons and $d = 18$ fm for equal partition of neutrons between fragments. Those values fairly well agree with the previously found $d = 22$ fm and 15 fm for the two respective cases.

It is difficult to directly relate the N/Z equilibration discussed in this paper to previous considerations of similar experimental results based on particle detection. We would like to refer in particular to two studies [15,22] that enable comparison of results as ^{64}Ni incident ions were used. In both of them, the evolution of the mean neutron-to-proton ratio was

measured as a function of the total energy loss during the collision. This quantity could not be observed in our experiment, since the established product distributions are integrated over all possible reaction dynamics. The total mass transfer is practically the only parameter which within a very crude approximation can be related to the total energy loss. Within this approximation one may conclude that results obtained in this work are in agreement with previously observed features. Even at a relatively small mass transfer between two colliding nuclei a partial N/Z equilibration is achieved and the effect gradually increases at larger mass transfers corresponding to larger total kinetic energy loss.

There are also some experimental characteristics of both methods that make them complementary. The mass and charge resolution in experiments based on the detection of fragments is much better for the light fragments than for the heavy ones. Consequently, the authors of such studies, usually discuss the evolution of the N/Z ratio for light reaction fragments only. In contrast to this, our method of analysis produces complete distributions of all products, independent on the considered mass range. The N/Z results derived from these distributions are even more complete and reliable for the heavy fragments. In this way the mass regions explored by both methods only partly overlap. The essential difference in applied techniques makes them independent and complementary.

It is worthwhile to emphasize yet another aspect, which relates to the angular selectivity of particle detection experiments. The usual procedure includes several measurements at fixed detection angles, the results are afterwards averaged applying appropriate weights and including extrapolations to angles not covered by experiment. To ensure that enough statistics are collected, usually only the angles near the maximum of the angular distributions for deep-inelastic collision products are chosen. Moreover, the fragments emitted at forward angles cannot be detected at all. In our thick target study the product distributions include all fragments produced in the target and stopped in the target material. The full integration of angular distribution is thus naturally achieved.

One should point out that to achieve a better resolution in the neutron-to-proton ratio equilibration study it is worthwhile to select incident ions that offer the largest scale for the N/Z variation, i.e., the ^{208}Pb ($N/Z = 1.54$) and ^{58}Ni ($N/Z = 1.07$) instead of ^{64}Ni ($N/Z = 1.29$). In both particle detection measurements mentioned above [15,22] the authors made comparative studies of the N/Z equilibration for ^{64}Ni and ^{58}Ni bombardments of heavy targets. In fact, we have also studied the ^{208}Pb + ^{58}Ni collisions at an energy above the Coulomb barrier comparable with the ^{64}Ni measurement. In addition we also analysed in an identical way the ^{130}Te + ^{64}Ni system for which the fusion evaporation and fusion–fission reactions contribute much more sizably to the total reaction cross section. Partial results of these analyses were already reported [13,14]. However, the full account of results and conclusions derived from the study of all three systems will be given in a subsequent publication.

6. Summary

We have applied the discrete gamma ray spectroscopy as a tool to investigate heavy ion collisions, with the primary aim to study the potential use of deep-inelastic processes for spectroscopy of neutron-rich nuclei inaccessible in standard fusion reactions. In

experiments multidetector gamma spectrometers were used to collect high statistics and high quality gamma coincidence data. We demonstrated that such experimental information supplemented by results of additional off-line radioactivity measurements is complete enough to reconstruct distributions of products of very complex nuclear reactions. The resulting maps of fragments are integral, since they include products of various nuclear processes, from quasielastic, few nucleon transfer to deep-inelastic, fusion-fission and fusion-evaporation reactions. In case of heavy ion collisions at energies slightly above the Coulomb barrier large ensembles of nuclear species are produced in deep-inelastic processes. The distribution of fragments obtained from such analysis is a perfect set of data to study the flow of mass and charge, which reflects the N/Z equilibration process, most important for the production of neutron-rich nuclei.

The gamma coincidence experiment and a complete analysis was performed for the ^{208}Pb + 350 MeV ^{64}Ni reaction at the collision energy approximately 12% above the barrier. The established distribution of fragments includes isotopes populated with cross sections varying from hundreds of millibarns down to tenths of microbarns. An average accuracy of the production yield determination of about 20% was reached.

We analysed cross coincidences between gamma transitions in specific partner fragments and estimated the neutron evaporation from primary excited products. By correcting the experimental map of final fragments for the evaporation of neutrons, we transformed it into the primary product distribution. The corrected experimental yield results were than used to study the equilibration of the N/Z ratio in deep-inelastic processes. Because of the intense exchange of mass and charge between the colliding nuclei, we could observe the equilibration effect over a wide range of mass.

The experimental results were compared with an equilibration formula derived from the liquid drop energy minimization for a system of two distant spherical nuclei. The fit results suggest that a considerable distance of 3 to 10 fm (depending on the data set) between the nuclear surfaces has to be introduced into the formula in order to reproduce the data. The distant sphere calculations simulate a system of two touching deformed nuclei and the distance reflects the magnitude of deformation. The same result was obtained from numerical minimization of the total energy of the binuclear system—a procedure that included experimental nuclear masses and a realistic Coulomb interaction of two deformed nuclei at the scission point. Therefore we argue that in the deep-inelastic processes in which a large number of nucleons is transferred, the fragments which are formed in the exit channel originate from substantial deformation of intermediate nuclei interacting during the time of nuclear contact.

The reaction mechanism of the deep-inelastic process was subject of extensive studies in the decades of the seventies and eighties (see, for instance, [11,23] and references therein). The huge amount of experimental information gathered over the years was sufficient to create a consistent description of those processes. Recently, the deep-inelastic processes call back the attention of experimentalists since they are regarded as a potential way of populating exotic neutron rich nuclei far off the stability path which cannot be produced in other reactions [18]. One of the goals of this study was to gain practical knowledge on how far the production of exotic nuclei can be extended. The N/Z ratio equilibration results show that in bombardments of a heavy target with a large neutron excess with a lighter neutron rich projectile, one can still transfer a considerable number of neutrons

into the light fragment, thus creating very exotic isotopes. For larger mass transfers the neutron evaporation effect starts to compete with the neutron-to-proton ratio equilibration and consequently, fragments which lie close to the stability path are formed. A considerable number of medium-light neutron rich nuclei may be exploited as projectiles to access and open interesting, previously inaccessible parts of the nuclidic chart for spectroscopic investigations.

Acknowledgements

References

[1] T. Pawłat, R. Broda, W. Królas, A. Maj, M. Ziębliński, H. Grawe, R. Schubart, K.H. Maier, J. Heese, H. Kluge, M. Schramm, Nucl. Phys. A 574 (1994) 623.

[2] R. Broda, B. Fornal, W. Królas, T. Pawłat, D. Bazzacco, S. Lunardi, C. Rossi Alvarez, R. Menegazzo, G. de Angelis, P. Bednarczyk, J. Rico, D. De Acuña, P.J. Daly, R.H. Mayer, M. Sferrazza, H. Grawe, K.H. Maier, R. Schubart, Phys. Rev. Lett. 74 (1995) 868.

[3] B. Fornal, R. Broda, W. Królas, T. Pawłat, J. Wrzesiński, D. Bazzacco, D. Fabris, S. Lunardi, C. Rossi Alvarez, G. Viesti, G. de Angelis, M. Cinausero, D.R. Napoli, Z.W. Grabowski, Phys. Rev. C 55 (1997) 762.

[4] C.T. Zhang, P. Bhattacharyya, P.J. Daly, Z.W. Grabowski, R.H. Mayer, M. Sferrazza, R. Broda, B. Fornal, W. Królas, T. Pawłat, D. Bazzacco, S. Lunardi, C. Rossi Alvarez, G. de Angelis, Nucl. Phys. A 628 (1998) 386.

[5] R. Broda, M.A. Quader, P.J. Daly, R.V.F. Janssens, T.L. Khoo, W.C. Ma, M.W. Drigert, Phys. Lett. B 251 (1990) 245.

[6] R. Broda, C.T. Zhang, P. Kleinheinz, R. Menegazzo, K.H. Maier, H. Grawe, M. Schramm, R. Schubart, M. Lach, S. Hofmann, Phys. Rev. C 49 (1994) 575.

[7] R. Bock (Ed.), Heavy Ion Collisions, North-Holland, Amsterdam, 1980.

[8] D.A. Bromley (Ed.), Treatise of Heavy Ion Science, Plenum, New York, 1980.

[9] W.J. Swiatecki, J. Phys. Colloq. C 5 33 (1972) 45.

[10] W. Nörenberg, J. Phys. Colloq. C 5 37 (1976) 141.

[11] W.U. Schröder, J.R. Huizenga, in: D.A. Bromley (Ed.), Damped Nuclear Collisions in Treaties of Heavy Ion Science, Vol. 2, Plenum, New York, 1984.

[12] H. Freiesleben, J.V. Kratz, Phys. Rep. 106 (1984) 1.

[13] W. Królas, Ph.D. Thesis, Institute of Nuclear Physics, Kraków, 1996, Report No. 1738.

[14] R. Broda, W. Królas, B. Fornal, T. Pawłat, K.H. Maier, H. Grawe, M. Schramm, R. Schubart, D. Bazzacco, S. Lunardi, C. Rossi Alvarez, G. de Angelis, P.J. Daly, C.T. Zhang, Z.W. Grabowski, Acta Phys. Hung. N.S. 7 (1998) 71.

[15] K. Sapotta, R. Bass, V. Hartmann, H. Noll, R.E. Renfordt, K. Stelzer, Phys. Rev. C 31 (1985) 1297.

[16] U. Reus, W. Westmeier, At. Data Nucl. Data Tables 29 (1983) 1.

[17] K.E. Rehm, C. Beck, A. van den Berg, D.G. Kovar, L.L. Lee, W.C. Ma, F. Videback, T.F. Wang, Phys. Rev. C 42 (1990) 2497.

[18] B. Fornal, R. Broda, W. Królas, T. Pawłat, P.J. Daly, I.G. Bearden, Z.W. Grabowski, R.H. Mayer, D. Nisius, L. Richter, M. Sferazza, M. Carpenter, R.V.F. Janssens, T.L. Khoo, T. Lauritsen, D. Bazzacco, S. Lunardi, C. Rossi Alvarez, G. de Angelis, P. Bednarczyk, H. Grawe, K.H. Maier, R. Schubart, Acta Phys. Pol. B 26 (1995) 357.

[19] R. Bock, Y.T. Chu, M. Dakowski, A. Gobbi, E. Grosse, A. Olmi, H. Sann, D. Schwalm, U. Lynen, W. Müller, S. Bjørnholm, H. Esbensen, W. Wölfli, E. Morenzoni, Nucl. Phys. A 388 (1982) 334.

[20] W.J. Swiatecki, private communication, 1995.

[21] A.H. Wapstra, G. Audi, R. Hoekstra, At. Data Nucl. Data Tables 39 (1988) 281.

[22] R. Płaneta, S.H. Zhou, K. Kwiatkowski, W.G. Wilson, V.E. Viola, H. Breuer, D. Benton, F. Khazaie, R.J. McDonald, A.C. Mignerey, A. Weston-Dawkes, R.T. de Souza, J.R. Huizenga, W.U. Schröder, Phys. Rev. C 38 (1988) 195.

[23] A. Gobbi, W. Nörenberg, in: R. Bock (Ed.), Dissipative Collisions in Heavy Ion Collisions, North-Holland, Amsterdam, 1980.